https://erjm.journals.ekb.eg
ISSN: 1110-1180

DOI: ---------

ERJ
Engineering Research Journal
Faculty of Engineering
Menoufia University

Implanted Rebars for Enhancing the Performance of CFST Column Embedded in RC Footings Under Cyclic Loads

Hossam M. Elkabsh*, Boshra A. Eltaly, Ghada M. Hekal

Department of Civil Eng., Faculty of Engineering, Menoufia University, Menoufia, Egypt
**(Corresponding author: hossam.moustafa4655@sh-eng.menofia.edu.eg)*

ABSTRACT
Concrete-filled steel tubes (CFSTs) offer a rapid and cost-effective construction method, providing superior strength and stiffness compared to reinforced concrete and structural steel. This study aims to enhance the performance of the CFST column embedded connection in reinforced concrete footings under cyclic loads using implanted rebars. The FEM program ANSYS 2023 R1 was employed for numerical analysis. The results demonstrate that the incorporation of implanted rebars within the critical section of the connection increases the moment capacity by a factor of 1.1-1.5 and ductility by a factor of 1.05-1.35, based on the reinforcement ratio and the rebars' development length inside the concrete core of the CFST column. These improvements are achieved while maintaining the same main characteristics, such as the diameter to thickness (D/t) ratio and the grade of both steel and concrete. These findings suggest a promising approach for improving the connection strength without incurring additional costs.

Keywords*: CFST; Cyclic load; Embedded base connection; Micro-plane model; coupled damage plasticity model.*

1. Introduction

In place of traditional reinforced concrete columns and bridge piers, concrete filled steel tubular (CFST) columns are composite structural elements that are effective and affordable. To maximize strength and stiffness and reduce weight and material needs, a steel tube is used to strengthen the concrete at the column outside perimeter. The concrete fill provides rigidity and prevents localized buckling of the steel tube while the steel tube restricts and strengthens the concrete fill. The steel tube sustains loads as construction advances during concrete curing, and the tube serves as formwork and support for the installation of concrete. Compared to reinforced concrete piers, CFSTs offer greater compressive strength, stiffness, and bending resistance, and they are subjected to less severe damage during seismic deformations [1,2]. Because there are few practical and affordable connections, there are few design provisions in the AASHTO, AISC, and ACI standards, CFSTs are not often employed in bridge construction [3-6]. CFST connections remain generally neglected, despite recent research leading to greater understanding and standardization of design expressions for CFST components. To get around this restriction, recent research has looked at a variety of CFST column-to-foundation and column-to-cap beam connections. These connections range from internal or exterior dowels extending from the CFST into the foundation or cap beam to embedded connections where the steel tube becomes embedded in the concrete of the foundation or cap beam [1,2,6–9].

This type of connection was subjected to extensive experimental studies [10-13]. The results reveal that the connections exhibit two possible failure mode depending on the embedment depth, as depicted in Figure (1) [14]. Pullout failure may occur when the embedment depth is insufficient, while punching shear failure may occur with shallow base depth below the CFST column. With adequate connection strength, both failure modes can be avoided, resulting in the desired ductile yielding of the column. Therefore, identifying all parameters that impact the failure modes of the connection (brittle pull-out failure or ductile failure of CFST pier or column) is crucial. Yet (Lehman and Roeder CW ,2012) [1,2] experimental research showed that setting the embedment depth to 0.9D is more than enough to guarantee that no cone pullout failure is likely to happen. The enhancement of connections of the embedded type is the primary objective of this study. A finite element (FE) model is developed using (Ansys 2023 R1) and verified with previous practical and numerical research. The verified model is then used to conduct a parametric study to find out to what extent the implanted rebars inside the concrete infill can affect the behaviour and strength of the embedded connection of the CFST. All columns are connected by an annular ring, which is welded to the end of the steel tube and inserted in the concrete of the foundation or cap beam with depth of 0.90D where D is the outer tube diameter [1,2,9]. Research has shown that implanted rebars can increase the flexural capacity of the CFST component and create significant ductility and strength when subjected to lateral loads as compared to the conventional embedded connections.

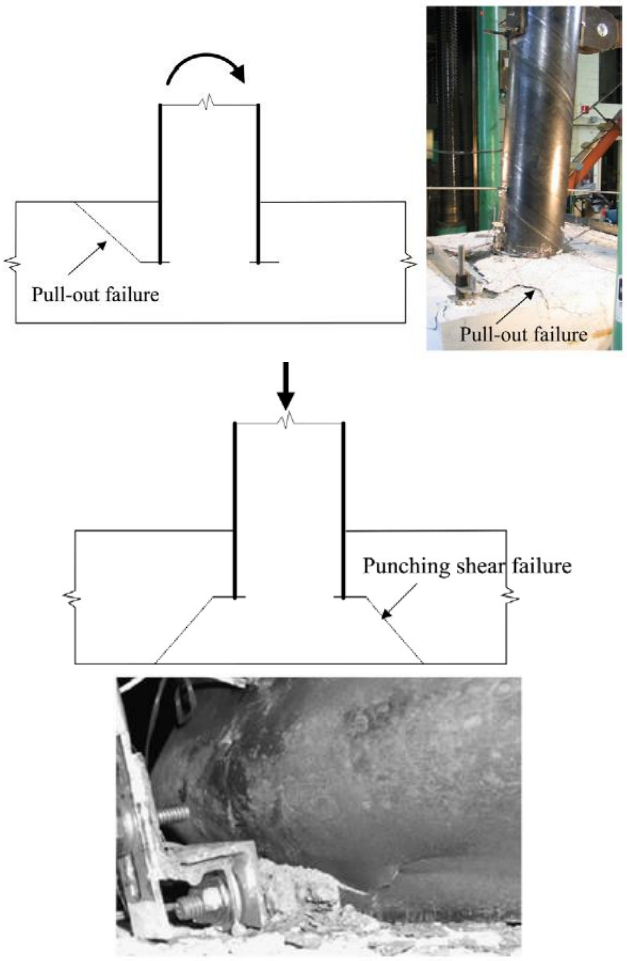

Figure 1- Embedded type connection failure modes

2. Finite element model

2.1 Material Models

Concrete material model:

The stress-strain behaviour of concrete governs its load-carrying capacity and ductility. In our case two types of stress strain curves are adopted. The conventional stress strain curve for concrete is used for the unconfined concrete of the footing while the confined concrete core behaviour can be estimated using formulas like the Saenz equation [15]. The Saenz model was developed by Eduardo Saenz in 1964 based on experimental data [16]. It is one of the earliest and simplest models to estimate the strength of steel tube confined concrete. The model expresses a linear relationship between the lateral confining pressure (σ_{lat}) provided by the steel tube and the increase in concrete compressive strength. This confinement depends on the steel depth-to thickness (D/t) ratios [17]. The difference between the conventional and the confined concrete stress strain curve is illustrated in Figure (2) [18]. The maximum compressive strength of the confined concrete can be obtained from Eq. (1) and Eq. (2) [16,17,19-21].

$$f_{cc} = f_c + k_1\,\sigma_{lat} \quad \text{Eq. (1)}$$

$$\varepsilon_{cc} = \varepsilon_c\,(1 + k_2\,(\tfrac{\sigma_{lat}}{f_c})) \quad \text{Eq. (2)}$$

Where:

f_c: Compressive strength of unconfined concrete

f_{cc}: Compressive strength of confined concrete

f_{cu}: Ultimate residual compressive strength of concrete

ε_c: Compressive strain in concrete at maximum stress f_c

ε_{cc} : Compressive strain in confined concrete at f_{cc} (maximum stress)

ε_{cu}: Compressive strain in confined concrete at ultimate residual stress f_{cu}

k_1 and k_2, defined as the confining factors, are constants and can be obtained from experimental data. Meanwhile, the constants k_1 and k_2 were set as 4.1 and 20.5($5k_1$) [22].

To simulate the non-linear behaviour of concrete buildings, the most recent 3-D eight-node CPT215 element, which was developed using this CDPM model in ANSYS software, will be a promising element. This component can remove numerical instability and mesh sensitivity. The CDPM model is based on research by Zreid and Kaliske Figure (3) [23-25]. The model's comprehensive description can be found in [26]. The CDPM does not show in ANSYS Workbench, however, it can be accessed by APDL commands.

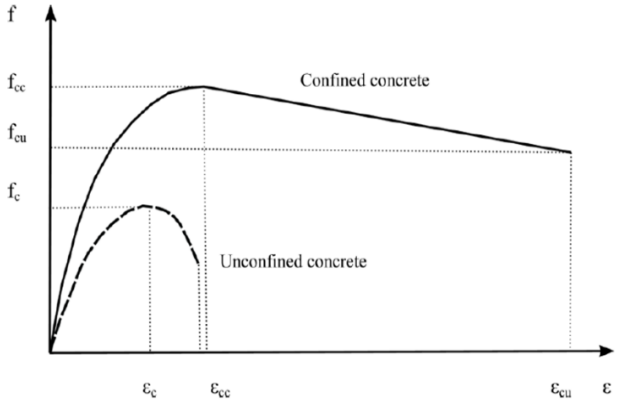

Figure 2- Compressive stress-strain relation of concrete

The 15 parameters needed for the CDPM model are listed in Table (1) [27-29]. And are obtained as follows:

1. Elasticity parameters: Young's modulus (E_c) for concrete is computed in the current study in accordance with the ACI 318-19 code [30] and Poisson's ratio is set to 0.20.

$$E_c = 4700\sqrt{f_c} \quad (MPa) \quad \text{Eq. (3)}$$

Where f_c , is the peak stress of concrete standard cylinder and the corresponding strain ε_c can be calculated from Eq. (4) proposed in [31].

$$\varepsilon_c = ((4 * f_c\ )\ ) / (3 * E_c\ ) \quad \text{Eq. (4)}$$

However, it is taken as 0.003 as recommended by the ACI318 and the ECP203 [30,32].

2. Plasticity parameters: The parameters f_c, f_{bc}, f_t are supposed to be obtained from experimental investigations. However, in cases of lacking test data, the following relations can be applied [27,33]:

$$f_{bc} = 1.15 * f_c \quad (MPa) \qquad \text{Eq. (5)}$$

$$f_t = 1.4 * \left(f_c/_{10}\right)^{\frac{2}{3}} \quad (MPa) \qquad \text{Eq. (6)}$$

The value σ_v^c which represents the intersection points between the compression cap and the Drucker-Prager function can be calculated from Eq. (7) [33]:

$$\sigma_v^c = -2/3 * f_{bc} \quad (MPa) \qquad \text{Eq. (7)}$$

The parameter R represents the ratio between the major and minor axes of the cap and is typically set to two [23]. The hardening parameter (D) is determined using Eq. (8), proposed by Nguyen and Houlsby [34].

$$f_{c0} = f_c\,(E_c + D)/E_c - D * \varepsilon_c \quad (MPa) \qquad \text{Eq. (8)}$$

Where:

f_{c0}: Found to be 30% f_c [29].

D: The hardening parameter

3. The damage parameters: The parameters $R_T, \beta_t, \gamma_{t0}$ are experimentally obtained through uniaxial cyclic tensile test. However, when there are no test data, R_T is typically set to one and β_t is assumed to be equal to $1.5\beta_c$. And since the softening in tension starts almost immediately after the elastic limit, γ_{t0} , the tension damage threshold, is logically assumed to equal Zero [23,28].

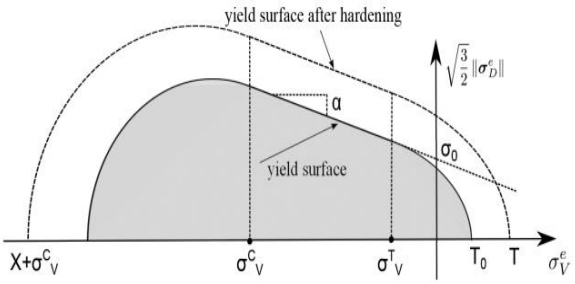

Figure 3- Smooth three-surface microplane cap yield function

The damage and hardening parameters are calibrated in the reasonable range to match the force-displacement curves experimentally [33]. To avoid the numerical instability of the solution due to the strain softening of the material, the nonlocal implicit gradient regularization method is counted on by adding two extra degrees of freedom for each node. In this method, two parameters, namely the over-nonlocal (m) and nonlocal interaction range (c), are defined.

Table 1- The parameters of the CDPM model

Parameter subtype	Parameter	Description	Units
Elasticity	E	The modulus of elasticity	MPa
	v	Poisson's ratio	-
Plasticity			
Dracker Prager yield function	fc	Uniaxial compressive strength	MPa
	fbc	Biaxial compressive strength	MPa
	ft	Uniaxial tensile strength	MPa
Compression cap	σ_v^c	The abscissa at the point of intersection between the compression cap and the Drucker Prager yield function.	MPa
	R	the ratio between the major and the minor axes of the cap	-
Hardening	D	Hardening material constant	MPa
	R_T	Tension cap hardening constant	-
Damage	γ_{t0} , γ_{c0}	Tension and compression damage threshold	-
	β_t , β_c	Tension and compression damage evolution constants	-
Nonlocal	c	Nonlocal interaction range parameter	mm^2
	m	Over-nonlocal averaging parameter	-

4. Nonlocal variables: Two extra degrees of freedom, namely the over-nonlocal (m) and nonlocal interaction range (c), are added at each node to prevent numerical instability of the solution due to the strain softening of concrete.

The solution is stable when the over-nonlocal averaging parameter, m, is greater than 1. Typically, m ranges from 1 to 3 and in this study, m is set to 2 [28,35]. The damage zone's resulting element size is determined by the nonlocal parameter c's possible values. Usually, the size should be in proportion to the size of the overall building. In this study the nonlocal parameter c is taken greater than $2l^2$ where (l) is the maximum element size in the FE model [23 and 28].

Steel material model:

The bilinear isotropic hardening material model within ANSYS Workbench was employed for the steel tube and reinforcing bars. The stress-strain behaviour was defined using a bilinear curve as described in Figure (4), with elastic modulus (E) of 200 GPa from tensile testing of steel samples. The post-yield hardening modulus (E_t), representing strain hardening in the plastic region, was estimated at 0.5% of the elastic modulus following the methodology in references [27 and 36].

A Poisson's ratio of 0.3 was defined for the steel tube and reinforcing bars in the finite element model, characterizing their lateral contraction under axial loading. This Poisson's ratio value is typically used for structural steel materials [14].

The reinforcing fibers were modelled using REINF264 elements [20, 29 and 37-39], which represent a uniaxially stiff spar with arbitrary orientation. Multiple fibers can be defined within one REINF264 element. The nodes, degrees of freedom and connectivity match the base element (CPT215). The REINF264 element can account for plasticity, stress stiffening, creep, large deflection, and large strain effects. [27, and 28]. As shown in Figure (5), REINF264 was used in conjunction with the 8-node CPT215 solid element to model reinforcing within the concrete footing and concrete core.

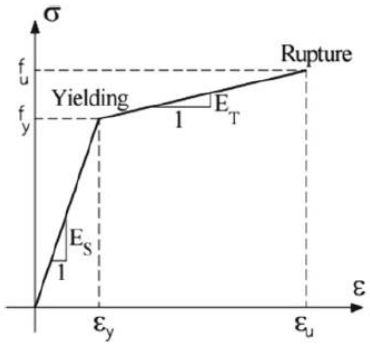

Figure 4- Bilinear stress strain curve for steel

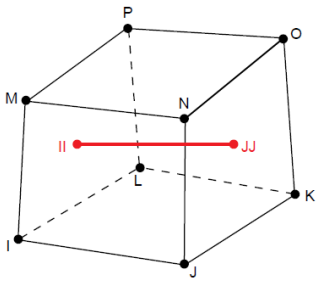

Figure 5- Geometry of Reinf264 element within 3D 8-Node Solid.

The steel tube in this study was modelled using the SOLID185 element, which is the default element for solid modelling in ANSYS. SOLID185 is a 3D solid element that represents solid structures and is characterized by 8 nodes, each with 3 translational degrees of freedom in the x, y, and z directions. This element, known for its plasticity, hyper elasticity, creep, and ability to handle large deformations, is particularly suitable for nonlinear static and dynamic analysis of solid structures [27, and 28].

2.2 Model Set-up and validation.

2.2.1 Model Geometry

The geometric parameters of the model were adopted from the references [1] and [14]. Detailed geometry dimensions are presented in Figure (6) and Figure (7). The depth of the RC footing is 609.6 mm, while the length of the footing in the direction of loading is 1930.4 mm, and in the transverse direction is 1727.2 mm. The footing is reinforced with #6 rebars, spaced 101.6 mm apart at the top and bottom in the loading direction. For the transverse reinforcement at the top and bottom, #4 rebars are utilized with a spacing of 228.6 mm. The outer diameter of the CFST column is 508 mm, and its tube has a thickness of 6.35 mm, resulting in a (D/t) ratio of 80. The clear height of the CFST column, measured from the top surface of the footing to the point of loading, is 1828.8 mm. The tube is embedded in the RC footing with an embedment depth of 0.90 times the diameter of the tube. To strengthen the connection and fix the tube temporarily during casting, an annular ring is welded to the end of the tube. This ring extends outside the tube by 16 times the thickness of the tube, and projects inside the tube by 8 times the thickness of the tube. Consequently, the width of the ring is 25 times the thickness of the tube.

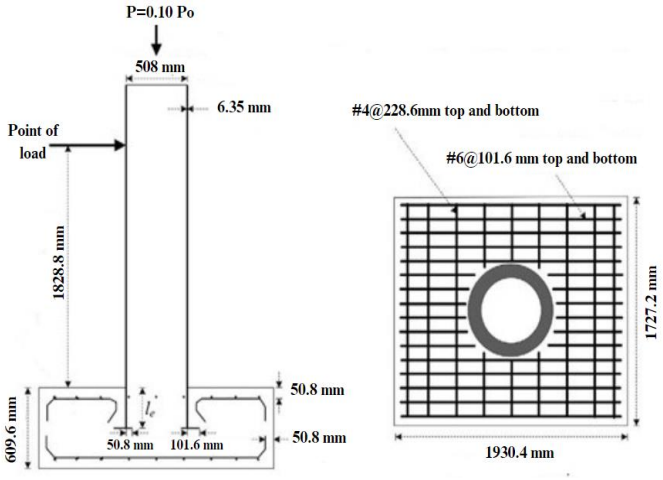

Figure 6- Model Geometry [14]

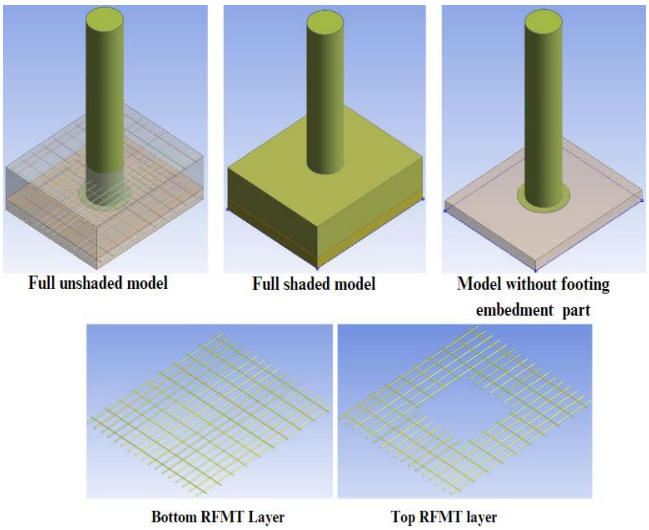

Figure 7- FEM model geometry in ANSYS

2.2.2 Material Models definition

The FE model in ANSYS was established based on previous experimental research conducted by Lehman (2012) [1] and analytical research utilizing ABAQUS by Moon (2013) [14]. Two samples, namely S1 and S2, were selected for analysis. These samples share identical geometries as shown in Figure (6) but differ in terms of the embedment depth. Sample S1 has an embedment depth of 0.60D, whereas sample S2 has an embedment depth of 0.90D.

The concrete characteristics of both samples are provided in Table (2). Additionally, different material models were employed for each sample. The material model details for samples S1 and S2 can be found in Table (3) and Table (4), respectively.

Table 2- Concrete properties for samples S1 and S2

Sample	$f_c(MPa)$	v
S_1	76	0.20
S_2	69	0.20

Table 3- The CDPM parameters for Concrete core and RC footing of Sample S1

Parameter subtype	Parameter	Value for CFST	Value for Footing
Elasticity	E	42870	41000
	v	0.20	0.20
Dracker Prager yield function	f_c	83.2	76
	f_{bc}	95.7	87.4
	f_t	5.75	5.4
Compression cap	σ_v^c	-63.8	-58
	R	2	2
Hardening	D	2E+04	2E+04
	R_T	1	1
Damage	γ_{t0}	0	0
	γ_{c0}	5.00E-05	5.00E-05
	β_c	2400	2400
	β_t	3600	3600
Nonlocal	c	16000	16000
	m	2	2

Table 4- The CDPM parameters for Concrete core and RC footing of Sample S2

Parameter subtype	Parameter	Value for CFST	Value for Footing
Elasticity	E	40974	39041
	v	0.20	0.20
Dracker Prager yield function	f_c	76	69
	f_{bc}	87.4	79.35
	f_t	5.4	5.07
Compression cap	σ_v^c	-58	-53
	R	2	2
Hardening	D	2E+04	2E+04
	R_T	1	1
Damage	γ_{t0}	0	0
	γ_{c0}	5.00E-05	5.00E-05
	β_c	2400	2400
	β_t	3600	3600
Nonlocal	c	16000	16000
	m	2	2

Steel with nominal yield strength of 520 MPa was used for the steel tube while steel grade 420 was used for the reinforcement rebars [41]. The properties of the two materials are presented in Table (5).

Table 5- Properties of Steel materials for samples S1 and S2

Element	$f_y(MPa)$	$f_u(MPa)$	E_s	v
Reinforcement	413	620	200000	0.30
Tube	520	605	200000	0.30

2.2.3 Boundary conditions

In ANSYS, the pressure load option was utilized to introduce a distributed axial load on the concrete section of the CFST in the first load step. Following this, starting from the second loading step, a distributed lateral displacement was applied to half the perimeter of the steel tube located at the CFST's top [14] as shown in Figure (8).

For the lateral load application, a cyclic history with multiple cycles at monotonically increasing drift levels was used. The conventional deformation history was performed based on ATC-24 protocol, as shown in Figure (9) [46].

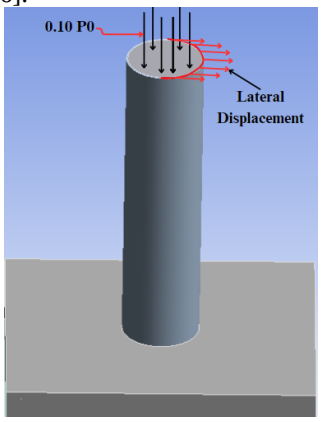

Figure 8- Load application manner in ANSYS Mechanical

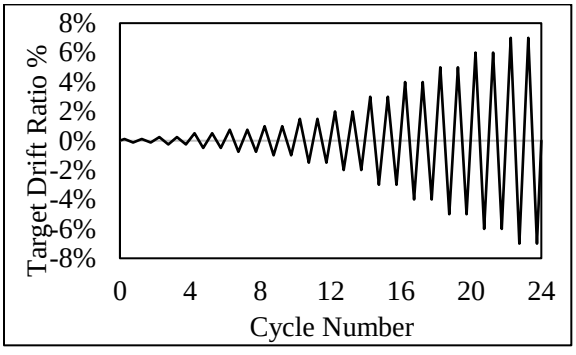

Figure 9- Standard Displacement Monotonic Cyclic History as per ATC-24

Supports were assigned to match the experimental set-up adopted in [1] and the ABAQUS model of the same test experiments investigated in [14]. Consequently, the bottom face of the RC footing was restrained in X, Y and Z directions by means of fixed support tool available in ANSYS as illustrated in Figure (10).

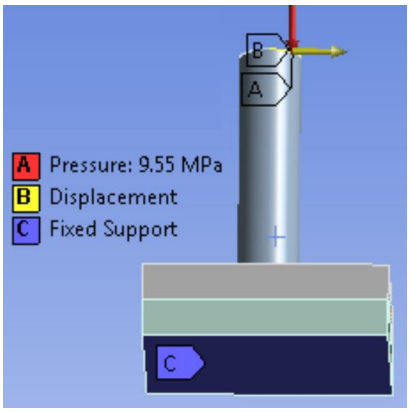

Figure 10- Model Boundary Conditions

2.2.4 Interface between steel tubes and concrete

A nonlinear frictional contact algorithm provided by ANSYS was utilized to accurately simulate the anticipated sliding and slip phenomena occurring at the interfaces between the concrete core and the steel tube, as well as between the steel tube and the concrete footing [40]. The CONTA174 and TARGET170 elements were employed to represent pair-based contact and sliding between 3D target surfaces and a deformable surface. These elements are highly suitable for 3D structural analyses and coupled-field contact analyses [28, 29, and 42].

Different friction coefficients were employed, and their corresponding simulation results were compared with experimental data to determine the optimal friction coefficient for subsequent parametric study. The validity of the findings obtained from varying friction coefficients was established by comparing them with experimental results presented in a study conducted by D. Lehman in 2012 [1]. Additionally, a comparison was made between these results and the ABAQUS simulation results presented in a study by J. Moon in 2013 [14], which also utilized the same experimental program. The comparisons between the ANSYS results, experimental results, and ABAQUS results are provided in Table (6) and Table (7), respectively. The maximum moment obtained from the experimental test, ANSYS model, and ABAQUS model are denoted by $M_{u,test}, M_{u,Ansys}, and\ M_{u,Abaqus}$ respectively.

The results are depicted in Figure (11), where the x-axis represents the percentage of drift, and the y-axis represents the maximum resisted lateral force. In this context, drift refers to the ratio between the maximum lateral displacement at the top of the column and the clear height of the CFST column, measured from the

surface of the RC footing to the point of application of the lateral load.

Table 6- A comparison between the FEM and experimental results with various friction coefficients

Specimen	$M_{u,Ansys}/M_{u,test}$ (F.C=0.10)	$M_{u,Ansys}/M_{u,test}$ (F.C=0.20)	$M_{u,Ansys}/M_{u,test}$ (F.C=0.30)	$M_{u,Ansys}/M_{u,test}$ (F.C=0.40)
S1	0.981	1.013	1.016	1.033
S2	0.983	0.990	0.997	0.986

Table 7- A comparison between ANSYS and ABAQUS results with various friction coefficients

Specimen	$M_{u,Ans.}/M_{u,Abaqus}$ (F.C=0.10)	$M_{u,Ans.}/M_{u,Abaqus}$ (F.C=0.20)	$M_{u,Ans.}/M_{u,Abaqus}$ (F.C=0.30)	$M_{u,Ans.}/M_{u,Abaqus}$ (F.C=0.40)
S1	0.972	1.015	1.017	1.035
S2	1.014	1.029	1.036	1.025

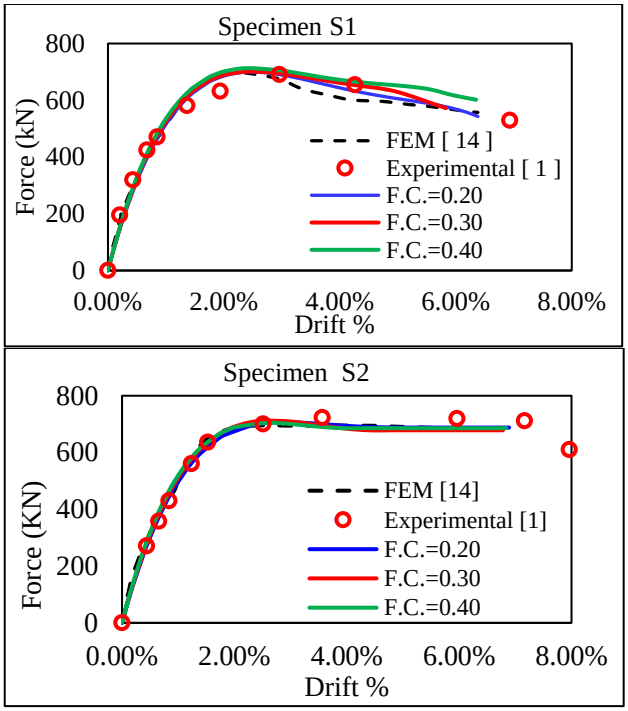

Figure 11- Comparison of predicted and measured lateral force vs. drift for different friction coefficients

The results of this study show that the friction coefficient has minimal influence on the behaviour of the CFST column under both static and cyclic loads, which is consistent with the findings reported by Gupta, P.K [20]. However, a friction coefficient of 0.30 was chosen for this investigation as it resulted in improved agreement with the post-peak behaviour of certain specimens, as shown in Figure (11).

2.2.5 Meshing

To conduct the analysis, a pure hexahedral mesh was employed as the basis for the computational model using the multizone meshing method available in ANSYS [44 and 45]. To determine the optimal mesh for use in the subsequent parametric study, three mesh configurations were examined and evaluated [14 and 43] as presented in Figure (12).

The investigation results presented in Table (8), Table (9), and Figure (13) indicate that the microplane model demonstrates both robustness and efficiency by showing insensitivity to changes in the mesh due to the non-local parameters [23-26]. The observed maximum deviation was less than 3%, which is considered negligible. However, among the meshes tested, mesh (1), the finest one, exhibited the closest agreement with experimental results in terms of the maximum lateral force. Consequently, it was selected for further parametric analysis

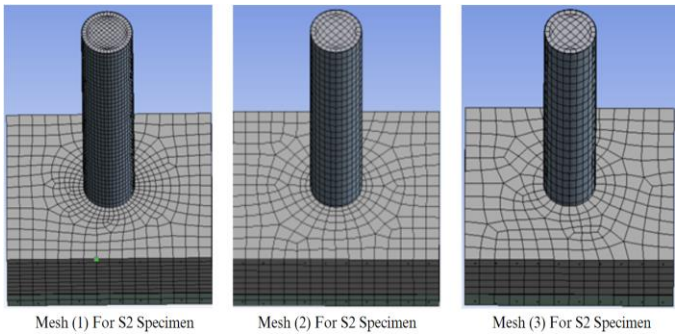

Figure 12- Different Meshes for analysis model

Table 8- Effect of different meshes in the cyclic load model (Verified with test results)

Specimen	$M_{u,Ansys}/M_{u,test}$ Mesh (1)	$M_{u,Ansys}/M_{u,test}$ Mesh (2)	$M_{u,Ansys}/M_{u,test}$ Mesh (3)
S1	1.016	1.012	0.988
S2	0.992	0.989	0.978

Table 9- Effect of different meshes in the cyclic load model (Verified with ABAQUS results)

Specimen	$M_{u,Ans.}/M_{u,Abaqus}$ Mesh (1)	$M_{u,Ans.}/M_{u,Abaqus}$ Mesh (2)	$M_{u,Ans.}/M_{u,Abaqus}$ Mesh (3)
S1	1.006	1.003	0.979
S2	1.031	1.028	1.016

Beside the agreement of the FEM results with the observed results of the experimental test [1] and the measured results from the ABAQUS model [14], the FEM showed a dramatic agreement with previous test results also in failure pattern. Figure (14) and Figure (15) show the agreement between the failure pattern of the specimen in experimental test, ABAQUS model and ANSYS model at the same drift level for samples S1 and S2, respectively.

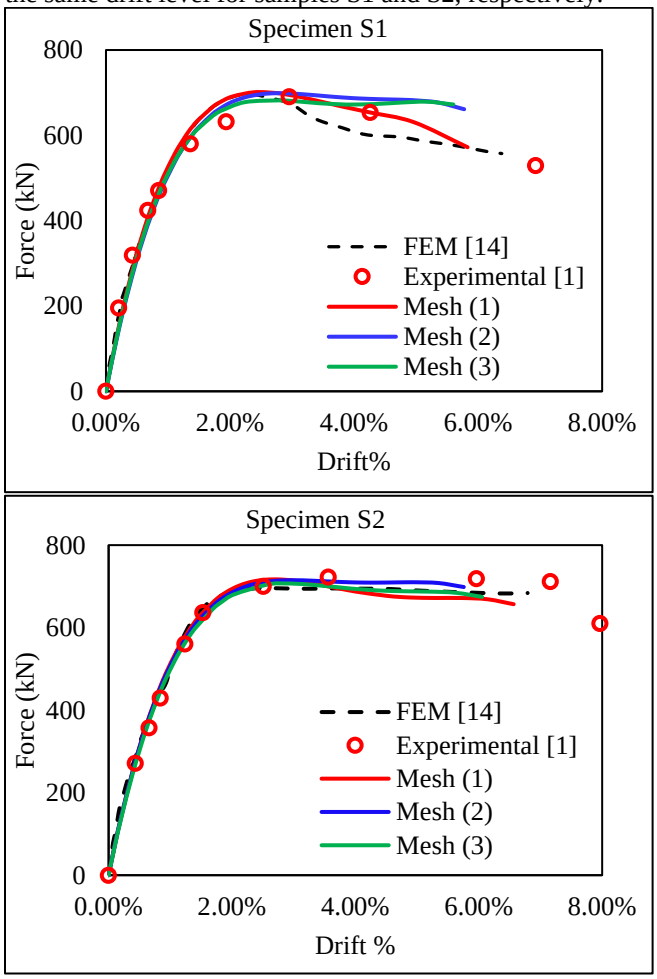

Figure 13- Comparison of predicted and measured lateral force vs. drift for different meshes.

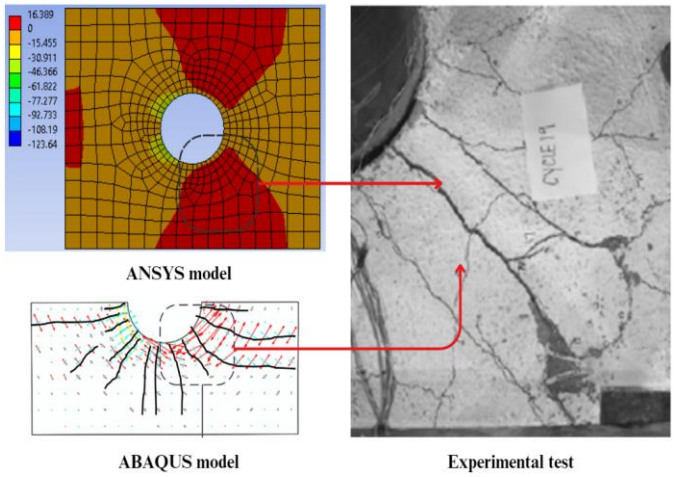

Figure 14- Simulated and observed damage patterns for specimen S1 at 5% drift level.

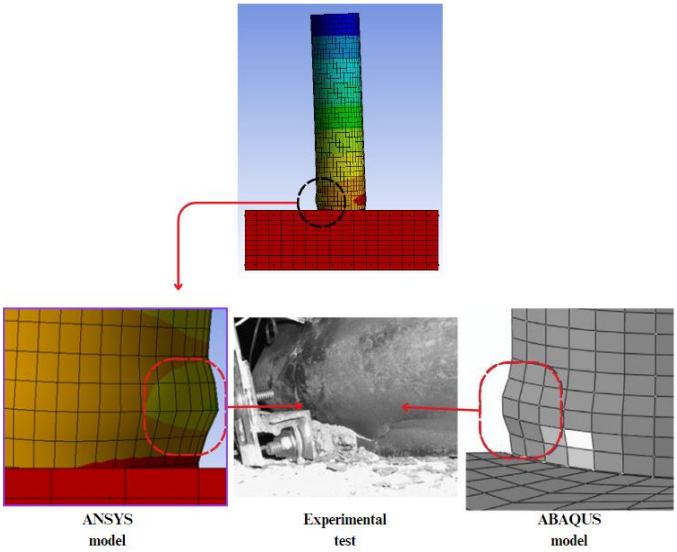

Figure 15- Simulated and observed damage patterns for specimen S2 at 6% drift level.

3. Parametric study

CFST columns are essential elements of bridges and high-rise buildings especially in high seismic zones. These structures are often subjected to cyclic stresses and plastic hinges are likely forming during seismic activities which make these elements necessary to have more capacity and ductility to withstand this type of loads by delaying the forming of local buckling of the tube. Therefore, the use of strengthening techniques that preserve the section and its external dimensions is the best option. Instead of increasing the CFST column overall diameter or increasing the diameter to width ratio (D/t), implanted rebars will be utilized to provide more interaction between the concrete core of the CFST and the RC footing.

This study aimed to study the behaviour of the CFST column reinforced by steel rebars only in the tube

buckling zone. The parametric study was conducted by utilizing the validated FEMs. A detailed parametric study is carried out to evaluate the effects of the reinforcement ratio of these rebars and length of the rebars development inside the concrete core. A total of 13 CFST columns divided into three groups were studied numerically up to failure. The groups and their studied parameters were tabulated in Table (10). All studied columns were constructed with identical geometric properties and reinforcement details as shown in Figure (6). All studied full scale CFST column-to-footing connection samples were based on the geometric details of sample S2 to avoid cone pullout failure by utilizing a 0.9D tube embedment depth.

The parametric numerical study comprised three distinct groups of CFST columns, each subject to varying reinforcement ratios and rebar development lengths within the tube. The first group consisted of four CFST columns reinforced with a 2% reinforcement ratio, comprising a total of 19 rebars with a diameter of 16 mm. The development lengths of the rebars within the tube were set to 20%, 30%, 40%, and 50% of the column clear height which was 1850 mm. Similarly, the second group comprised four CFST columns reinforced with a 4% reinforcement ratio, equipped with 21 rebars measuring 22 mm in diameter, and subjected to the same development lengths. The third group consisted of five CFST columns reinforced with a 6% reinforcement ratio, containing 23 rebars with a diameter of 25 mm. Rebar development lengths within the tube were set to 20%, 30%, 40%, 50%, and 60% of the column clear height above the concrete footing.

To ensure consistent behaviour across all specimens, the rebars employed in each case featured a 90^0 hook configuration with a length of 300 mm, resulting in a development length of 850 mm. Detailed parameters can be found in Figure (16), which provides a graphical representation of the investigated parameters.

For the construction of the models, the same configurations of the verified Finite Element (FE) ANSYS model were adopted, employing the REINF264 element to accurately simulate the behaviour of the implanted rebars. This modelling approach was consistent across all specimens, including the top and bottom reinforcement layers.

The primary objective of this comprehensive investigation was to identify the most effective configuration of implanted rebars capable of enhancing the connection capacity between CFST columns and footings while optimizing the overall structural behaviour.

Table 10- Parametric study samples details

Group	Sample	Num. of rebars	Rebars diameter (mm)	L_d (mm)	Embedment depth
G1	R2%-H20%	19	16	370	0.90 D
	R2%-H30%	19	16	555	0.90 D
	R2%-H40%	19	16	740	0.90 D
	R2%-H50%	19	16	925	0.90 D
G2	R4%-H20%	21	22	370	0.90 D
	R4%-H30%	21	22	555	0.90 D
	R4%-H40%	21	22	740	0.90 D
	R4%-H50%	21	22	925	0.90 D
G3	R6%-H20%	23	25	370	0.90 D
	R6%-H30%	23	25	555	0.90 D
	R6%-H40%	23	25	740	0.90 D
	R6%-H50%	23	25	925	0.90 D
	R6%-H60%	23	25	1110	0.90 D

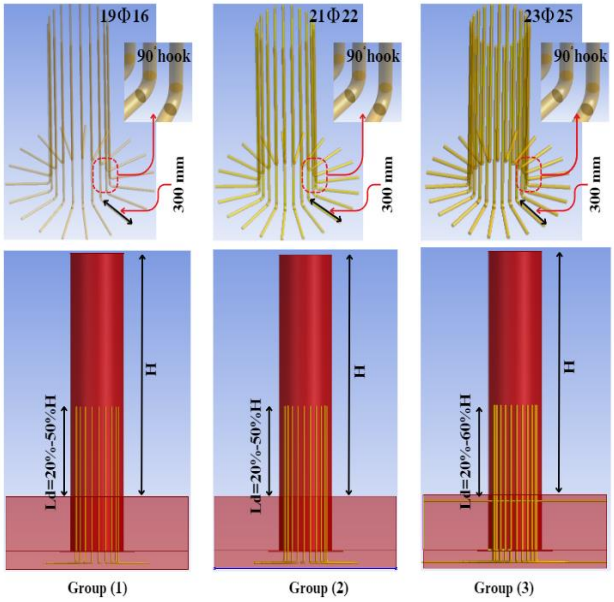

Figure 16- Illustration of the studied parameters of all 13 specimens

The studied strengthened groups were specifically designed to evaluate the optimal configuration of implanted rebars, aiming to achieve significant improvements in the CFST column-to-footing connection capacity and overall structural performance.

The utilization of the novel CFST column embedded connection with implanted rebars offers an intriguing alternative to costly solutions such as increasing the column diameter or reducing the (D/t) ratio. Its durability performance, combined with the potential for increased capacity in the CFST column

embedded connection, positions the implanted rebars technique as a highly cost-efficient solution.

The results for these FEMs were compared with the control sample S2 to investigate the effect of the implanted rebars and their length. The samples were organized into four distinct groups, each comprising a specific number of samples as presented in Table (11). The first group, denoted as G_0, served as the control group, and consisted of a single sample for comparative purposes. Meanwhile, groups $G_1, G_2, and\ G_3$ contained multiple samples, all possessing the same reinforcement ratio within their respective groups but with varying lengths of development (L_d).The moment resistance ratio (M_u/M_{s_2}) and the ductility index (D) were chosen to be compared for all specimen as a clear indicator for comparison and determination of the behavior of CFST column embedded connection. Where M_u is the maximum resisted bending moment of each sample and M_{s_2} is the maximum resisted bending moment in the control sample, S2 which was found to be 1317 kN.m according to the verified model and according to experimental tests [1] and prior finite element analysis [14]. The ductility index, D, is the ratio between the lateral displacement at the peak load, Δ_{peak}, to the lateral displacement at the yielding point of the steel tube, Δ_y [47]. The tube yielding was found to occur at a drift ratio of 1.3% and this value varied slightly for all specimens, however this variance was negligible. Therefore, the 1.3% drift ratio was set to be the yielding point of all specimens.

4. RESULTS AND DISCUSSION

It is evident that the introduction of implanted rebars significantly affects the resistance to bending moments in CFST columns. Group G1, with a reinforcement ratio of 2%, demonstrated an improvement in resistance and ductility compared to the control sample. Among the G1 samples, R2%-H30% displayed the highest enhancement, with a M_u value of 1485.05 kN.m, representing a 12.7% increase and 17% increase in ductility compared to the control sample. It can be noticed that with 370 mm (20% of column clear height) development length inside the core the moment capacity gained 8.7% and the ductility increased by 5%. It is worth mentioning that with longer development length than 30% of column height, no additional improvement was observed neither in strength nor in ductility. Moving to group G2, which featured a higher reinforcement ratio of 4%, the resistance to bending moments was further improved. The sample R4%-H30% demonstrated the highest increment, with an M_u value of 1658.25 kN.m, signifying a significant 25.7% increase compared to the control sample. This result highlights the substantial effect of higher reinforcement ratios on strengthening the structural capacity of CFST columns. Furthermore, sample R4-H30% possessed 17.2% increase in ductility which is almost the same increase in samples R2-H30%, R2-H40%, R2-H50%, R4-H40%, and R4-H50%. And the same as group G1, no additional significant improvement in strength and ductility was observed.

Similarly, within group G3, where the reinforcement ratio was set at 6%, the resistance to bending moments was further improved. Specifically, the sample labeled R6%-H50% exhibited a moment capacity (M_u) of 1935.96 kN.m, representing a significant increase of 46.7% compared to the control sample. This improvement is nearly double the effect observed with a 4% reinforcement ratio. Likewise, the sample R6%-H60% demonstrated a moment capacity of 1970.06 kN.m, corresponding to a remarkable enhancement of 49.8%. These results highlight the substantial influence of both higher reinforcement ratios and longer development lengths on the structural strength of CFST columns.

In addition to evaluating the resistance to bending moments, the ductility ratio provides insights into the ability of CFST columns to undergo deformation without experiencing significant loss of strength. Notably, samples within group G3 that possessed a 6% reinforcement ratio, particularly R6%-H50% and R6%-H60%, exhibited the highest levels of ductility. These samples displayed a significant increase in deformation capacity compared to the control sample. It is worth mentioning that unlike groups G1 and G2, where no additional improvement was observed beyond a development length of 555 mm (30% of column height), the strength and ductility of group G3 continued to increase with the elongation of the development length up to 1110 mm. Detailed results of the parametric study are presented in Table (11) and visualized in Figure (17), 18, and 19.

Furthermore, the findings indicated that for implanted rebars with a reinforcement ratio of 2% and a development length of 370 mm (R2%-H20%), the moment capacity increased by a modest 8.5%. Moreover, higher reinforcement ratios had no impact on the strength of the connection if the development length did not exceed 20% of the column clear height, as illustrated in Figure (20). However, it was observed that implanted rebars achieved their optimal effect when the development lengths reached 40% of the CFST column clear height, except for high reinforcement ratios (e.g., group G3), which required greater development lengths of up to 60% of the clear height to maximize their contribution to strength and ductility, as depicted in Figure (21).

Table 11- Numerical Results

Group	Sample	M_u $(KN.m)$	$\frac{M_u}{M_{us_2}}$	Δ_{peak} (mm)	Δ_y (mm)	Ductility (D) Δ_{peak}/Δ_y	Ductility Ratio D_i/D_{s_2}
G_0	S2	1317.11	1	46.67	24.05	1.94	1
G_1	R2%-H20%	1432.25	1.087	49	24.05	2.037	1.05
	R2%-H30%	1485.05	1.127	54.51	24.05	2.267	1.169
	R2%-H40%	1495.74	1.135	54.51	24.05	2.267	1.169
	R2%-H50%	1492.84	1.133	54.51	24.05	2.267	1.169
G_2	R4%-H20%	1482.48	1.126	52.50	24.05	2.183	1.125
	R4%-H30%	1658.25	1.26	54.7	24.05	2.274	1.172
	R4%-H40%	1706.31	1.295	54.7	24.05	2.274	1.172
	R4%-H50%	1706.34	1.296	54.7	24.05	2.274	1.172
G_3	R6%-H20%	1504.07	1.142	52.50	24.05	2.183	1.125
	R6%-H30%	1624.84	1.234	54.72	24.05	2.275	1.173
	R6%-H40%	1892.74	1.437	55.1	24.05	2.291	1.18
	R6%-H50%	1935.96	1.47	62.90	24.05	2.615	1.348
	R6%-H60%	1970.06	1.496	63.22	24.05	2.629	1.355

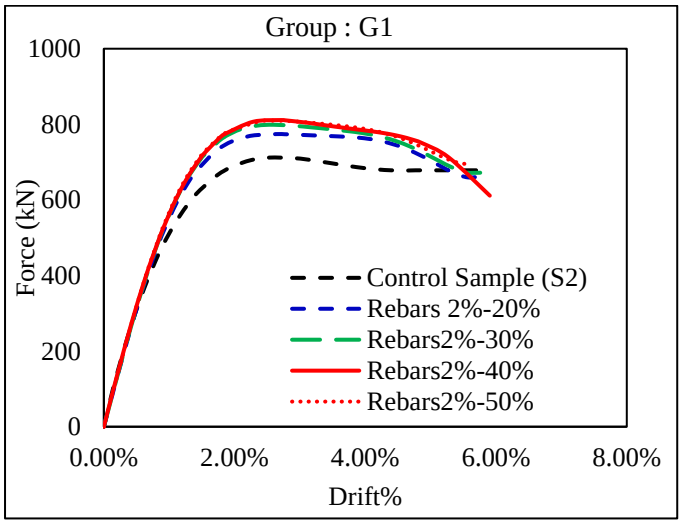

Figure 17- Effect of development length for 2% reinforcement ratio of implanted rebars

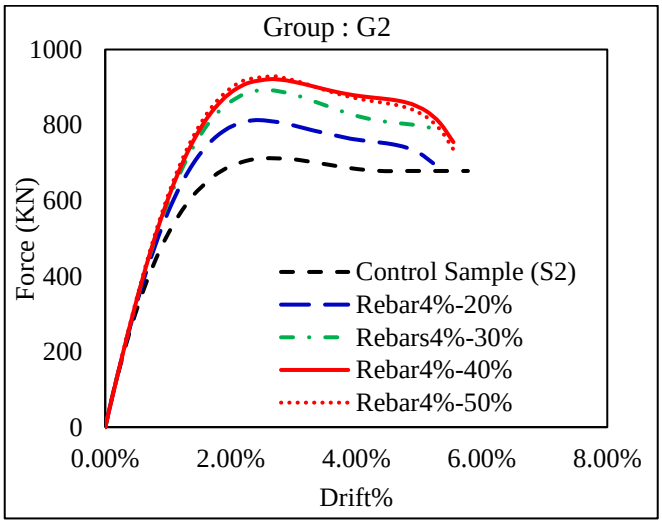

Figure 18- Effect of development length for 4% reinforcement ratio of implanted rebars

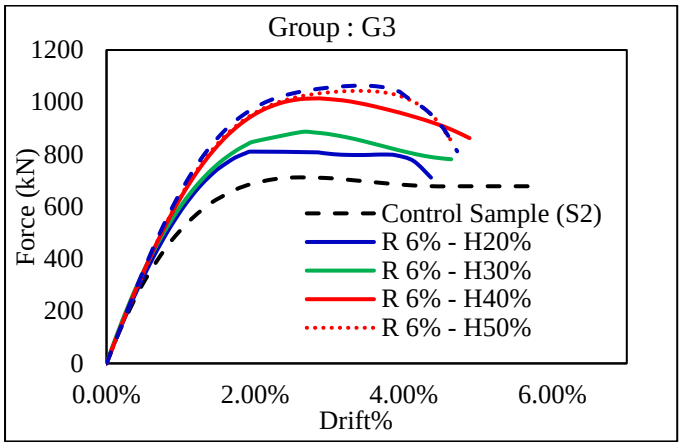

Figure 19- Effect of development length for 6% reinforcement ratio of implanted rebars

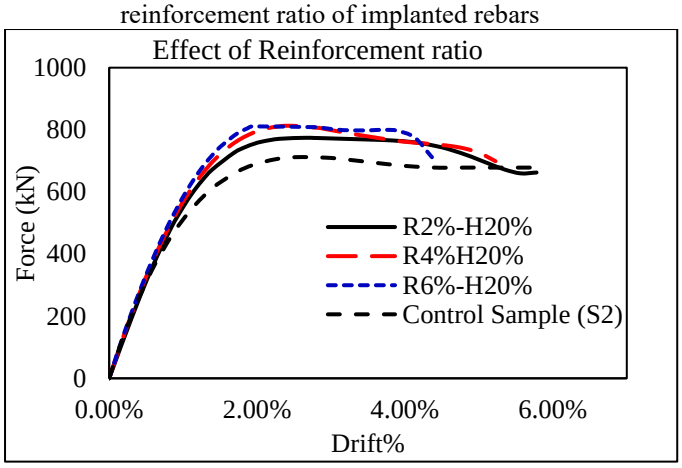

Figure 20- Effect of different reinforcement ratios with 20%H development length

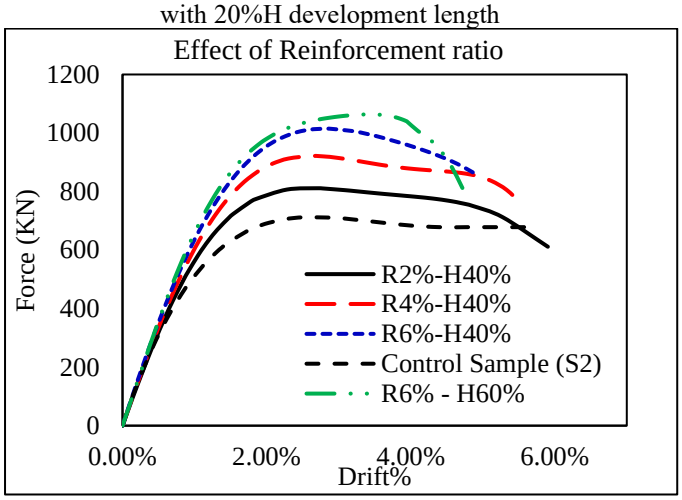

Figure 21- Optimal effect of different implanted rebars' ratios

Furthermore, to visualize the influence of the development length, a chart was generated to predict the impact of various development lengths on different ratios of implanted rebars. This chart, depicted in Figure (22), serves to enhance future design procedures by identifying the optimal combination of rebar ratios and their corresponding development lengths to achieve the maximum enhancement in moment capacity beyond the values obtained from conventional design approaches outlined in [1, 3, 14, and 41]. In this chart, the abscissa represents the ratio of development length to column height, while the ordinate represents the additional ratio of moment capacity that can be achieved beyond the capacity of a conventional CFST section without implanted rebars. The chart thus provides a visual tool for designers to determine the most suitable rebar ratio and development length combination to maximize the moment capacity of the CFST section when utilizing implanted rebars.

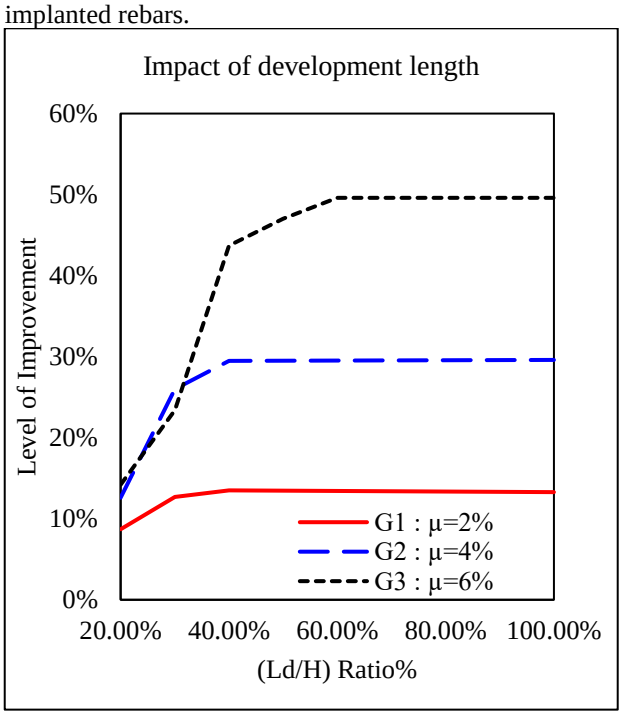

Figure 22- Level of improvement of connection based on the development length of implanted rebars for different rebars' ratios.

5. SUMMARY AND CONCLUSIONS

This study presents a numerical simulation and analysis of the embedded connection between a CFST column and its RC footing, where the connection is strengthened by implanted rebars with varying reinforcement ratios and development lengths. The connections were subjected to static vertical loading equivalent to 10% of the CFST column capacity, as well as cyclic monotonic lateral loading following the ATC24 procedure. The accuracy of the FE modelling was validated by comparing the FE results with experimental and numerical data from previous research on two CFST column embedded connections. The results of this study demonstrate that the FE modelling can effectively simulate the behaviour of the CFST column to footing connection. Specifically, the parametric study evaluated the effects of implanted rebars between the concrete core of the CFST column and the footing under applied loads. The key findings of this research can be summarized as follows:

1. The FE model accurately predicts the main behavior of the CFST column to footing connection

strengthened with implanted rebars under applied loads.

2. The coupled damage-plasticity model implemented in ANSYS using element CPT215 for concrete modelling and element REINF264 for reinforcement modelling proves to be highly effective in simulating the behavior of concrete, exhibiting non-mesh sensitivity.
3. The structural performance of the CFST column to footing connection is improved by the addition of implanted rebars. The ultimate capacity of the connection significantly increases by approximately 9-50% in the examined groups, while the ductility increases by 5-35% depending on the reinforcement ratio and development length of the implanted rebars.
4. Most reinforcement ratios of the implanted rebars reach their maximum contribution to the strength and ductility when the development length reaches 40% of the column clear height.
5. If the development length is less or equal to 20% of the column height, the strength and ductility increase by 8.7% and 5% respectively with rebars' ratio of 2% and no further improvement occurs for any grater rebar ratio.

6. REFERENCES

[1] Lehman, D.E., & Roeder, C.W. (2012). Foundation connection for circular concrete filled tubes. Journal of Constructional Steel Research, 78, 212-225.

[2] Lehman, D.E., & Roeder, C.W. (2012). Rapid construction of bridge piers with improved seismic performance. Report for the California department of transportation. Report number CA12-1972.

[3] AASHTO. (2015). AASHTO LRFD bridge design specifications. U.S. customary units with 2015 interim revisions. Washington, DC: American Association of State Highway and Transportation Officials, 7th edition.

[4] AISC. (2011). Steel construction manual. 14th edition. Chicago, IL: American Institute of Steel Construction.

[5] ACI 318. (2011). Building code requirements for structural concrete. Farmington Hills, MI: American Concrete Institute.

[6] Hsu, H., & Lin, H. (2003). Performance of concrete-filled tube base connections under repeated loading. In Proceedings of the International Workshop on Steel and Concrete Composite Construction (IWSCCC-2003). Report No. NCREE-0-0.26. Taipei, Taiwan: National Center for Research in Earthquake Engineering.

[7] Hitaka, T., Suita, K., & Kato, M. (2003). CFST column base design and practice in Japan. In Proceedings of the International Workshop on Steel and Concrete Composite Construction (IWSCCC-2003). Report No. NCREE-0.-0.26. Taipei, Taiwan: National Center for Research in Earthquake Engineering.

[8] Kappes, L., Berry, M., & Stephens, J. (2013). Performance of steel pipe pile-to-concrete cap connections subject to seismic or high transverse loading: phase III confirmation of connection performance. Montana State University. Report Number FHWA/MT-13-001/8203.

[9] Stephens, M.T., Lehman, D.E., & Roeder, C.W. (2015). Concrete-filled tube bridge pier connections for accelerated bridge construction. Report for the California Department of Transportation. Report Number CA15-2417.

[10] Kingsley, A. (2005). Experimental and analytical investigation of embedded column base connections for concrete-filled high-strength steel tubes. Master's thesis. Seattle, WA: University of Washington.

[11] Williams, T.S. (2006). Experimental investigation of high-strength concrete-filled steel tubes in embedded column base foundation connections. Seattle, WA: University of Washington.

[12] Chronister, A. (2007). Experimental investigation of high-strength concrete-filled steel tubes in embedded column base foundation connections. Master's thesis. Seattle, WA: University of Washington.

[13] Lee, J.R. (2011). Experimental investigation of embedded connections for concrete-filled steel tube columns subjected to combined axial-flexural loading. Master's thesis. Seattle, WA: University of Washington.

[14] Moon, J., Lehman, D.E., Roeder, C.W., & Lee, H.E. (2013). Evaluation of embedded concrete-filled tube (CFT) column-to-foundation connections. Engineering Structures, 56, 22-35.

[15] Saenz, L.P. (1964). Discussion of tests of compressed concrete cylinders confined by spiral reinforcement. ACI Journal Proceedings, 61(6), 729-739.

[16] Richart, F.E., Brandtzaeg, A., & Brown, R.L. (1929). A study of the failure of concrete under combined compressive stresses. Engineering Experiment Station Bulletin, 185, 1-110.

[17] Mander, J.B., Priestley, M.J.N., & Park, R. (1988). Theoretical stress-strain model for confined concrete. Journal of Structural Engineering, ASCE, 114(8), 1804-1826.

[18] Mirmiran, A., Zagers, K., & Yuan, W. (2000). Nonlinear finite element modeling of concrete confined by fiber composites. Finite Elements in Analysis and Design, 35(1), 79-96.

[19] Jayalakshmi, S., & Jayasankar, J.S. (2016). Finite element analysis and codal recommendations of concrete. Journal of the Institution of Engineers (India), 96(1), 33-41.

[20] Gupta, P.K., & Ahmed, Z. (2014). Modelling, verification, and investigation of behaviour of circular CFST columns. Structural Concrete.

[21] Eltaly, B., & Boshra, A. (2017). Structural behavior of recycled aggregates concrete-filled steel tubular columns. Challenge Journal of Concrete Research Letters.

[22] Patton, M.L., & Singh, K.D. (2014). Finite element modeling of concrete-filled lean duplex stainless steel tubular stub columns. International Journal of Steel Structures, 14(3), 619-632.

[23] Zreid, I., & Kaliske, M. (2018). Gradient enhanced plasticity-damage microplane model for concrete. Computational Mechanics, 62, 1239-1257.

[24] Zreid, I., & Kaliske, M. (2014). Regularization of microplane damage models using an implicit gradient enhancement. International Journal of Solids and Structures, 51, 3480-3489.

[25] Zreid, I., & Kaliske, M. (2016). Implicit gradient formulation for microplane Drucker-Prager plasticity. International Journal of Plasticity, 83, 252-272.

[26] Pirker, M. (2020). Non-linear seismic analysis of a concrete gravity dam using a microplane material model. Graz University of Technology. (Master's thesis)

[27] ANSYS Inc. (2023). ANSYS Mechanical APDL material reference. Release 2023.

[28] ANSYS Inc. (2023). ANSYS Mechanical APDL Theory Reference. Release 2023.

[29] Al, A.K. (2021). Finite element simulation on flexural behavior of RC slabs using coupled damage-plasticity microplane model. In Sustainable Civil Engineering and Architecture (pp. 825-836). Ho Chi Minh City, Vietnam.

[30] ACI. (2019). ACI 318-19: Building code requirements for structural concrete and commentary. Farmington Hills, MI: American Concrete Institute.

[31] Feenstra, P.H., & Borst, R.D. (1996). A composite plasticity model for concrete. International Journal of Solids and Structures, 33(5), 707-730.

[32] E.C.P. 203/2020. (2020). Egyptian code of practice: design and construction for reinforced concrete structures. Cairo, Egypt: Research Centre for Houses Building and Physical Planning.

[33] Jiang, H., & Zhao, J. (2015). Calibration of the continuous surface cap model for concrete. Finite Element Analysis and Design, 97, 1-19.

[34] Nguyen, G.D., & Houlsby, G.T. (2008). A coupled damage-plasticity model for concrete based on thermodynamic principles: Part I: model formulation and parameter identification. International Journal for Numerical and Analytical Methods in Geomechanics, 32, 353-389.

[35] Grassl, P., & Jirásek, M. (2006). Plastic model with non-local damage applied to concrete. International Journal for Numerical and Analytical Methods in Geomechanics, 30, 71-90.

[36] Pham, D.D., Nguyen, P.C., Nguyen, D.L., & Le, H.A. (2020). Simulation of concrete-filled steel box column. In J. Reddy, C. Wang, V. Luong, & A. Le (Eds.), ICSCEA 2019 (Lecture Notes in Civil Engineering, Vol. 80). Singapore: Springer.

[37] Mohamed Ali, I.Z. (2021). Design and construction of smart cities: Modeling of a reinforced concrete column under cyclic shear loads by a plasticity-damage microplane formulation (pp. 24-32). Cairo: Springer Nature Switzerland AG.

[38] Parvin, M.A. (2022). Finite element analysis of axially loaded RC walls with openings strengthened using textile reinforced mortar for sustainable structures. Buildings.

[39] Negassa, F. (2020). Numerical investigation of reinforced concrete columns with transverse holes. Global Scientific Journals.

[40] ANSYS Inc. (2023). ANSYS Mechanical APDL contact technology guide. Release 2023.

[41] AISC. (2010). Specification for structural steel buildings. Chicago, IL: American Institute of Steel Construction.

[42] ANSYS Inc. (2023). ANSYS Mechanical APDL Element Reference. Release 2023.

[43] Zreid, I., & Kaliske, M. (2018). A cyclic triaxial concrete microplane model with gradient regularization. In Computational Modelling of Concrete Structures (EURO-C 2018) (pp. 413-420). Bad Hofgastein, Austria: Taylor & Francis Group, London.

[44] ANSYS Inc. (2021). ANSYS Mechanical User's Guide. Release 2021.

[45] ANSYS Inc. (2023). ANSYS Meshing User's Guide. Release 2021.

[46] ATC-24. (1992). Guidelines for testing steel components. Redwood City, CA: Applied Technology Council.

[47] Salem Khalaf, F. Abed, & Alhoubi, Y. (January 2023). Flexural behavior of circular concrete filled steel tubes with partially incorporated demolished concrete lumps. Composite Structures - Composites Part C: Open Access, 10, 100346.